Influence of injected ions on α' formation under ion irradiation in Oxide Dispersion Strengthened Steels

Marie Loyer-Prost, Stéphanie Jublot-Leclerc, Marie-José Saleh-Afif, Joël Ribis, Aurélie Gentils

Influence of injected ions on α' formation under ion irradiation in Oxide Dispersion Strengthened Steels

Marie Loyer-Prost[1*], Stéphanie Jublot-Leclerc[2], Marie-José Saleh-Afif[1,2], Joël Ribis[3], Aurélie Gentils[2]

[1] Université Paris-Saclay, CEA, Service de recherche en Corrosion et Comportement des Matériaux, SRMP, F-91191, Gif-sur-Yvette, France

[2] Université Paris-Saclay, CNRS/IN2P3, IJCLab, 91405 Orsay, France

[3] Université Paris-Saclay, CEA, Service de Recherches en Matériaux et procédés Avancés, 91191 Gif-sur-Yvette, France

* marie.loyer-prost@cea.fr

*Corresponding author: Marie LOYER-PROST.

Mail: marie.loyer-prost@cea.fr

Courrier: CEA Saclay, DES/ISAS/DMN/SRMP/JANNUS (Bât 126, pièce 58), PC. 162, 91191 Gif-sur-Yvette CEDEX, France.

Telephone +33 (0)1 69 08 85 08.

Abstract (150 words):

Oxide Dispersion Strengthened (ODS) steels hold great promise for applications in next generation reactors. Under irradiation, a phase separation α/ α' can occur within the Fe-Cr matrix of ODS steels that can alter their mechanical properties. This work presents, for the first time, the characteristics of α' precipitates enhanced by ion irradiation at 400°C and examines the influence of the implanted ions. Far from the implanted region, α' is reported in significant density while at the implanted peak, the α' density is considerably reduced. This suggests that ion implantation either reduces the fraction of α' phase formed after irradiation or delays considerably its formation. Through atom probe tomography analysis and comparison with existing literature, the low impact of the damage rate and fluence on the α' formation in ODS steels is highlighted. Interestingly, the efficiency of ballistic mixing of α' appears to be less pronounced in ODS steels than in Fe-Cr systems.

Graphical abstract:

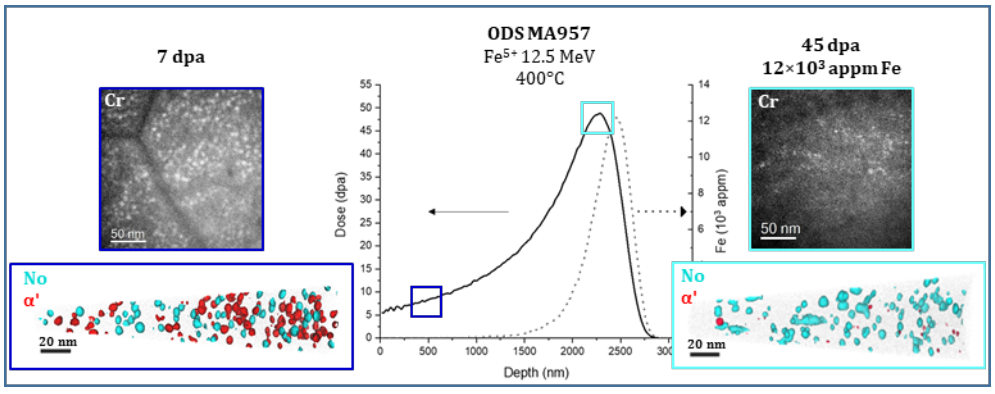

Oxide Dispersion Strengthened steels are promising materials for fuel element cladding of future Sodium-cooled fast neutron reactors and as plasma-facing material in the first wall of fusion reactors. Their Fe-Cr matrix is reinforced with a high density (10^{23} precipitates/m^3) of small nano-oxides of yttrium and titanium. Thanks to these nano-oxides, they exhibit good creep properties under irradiation and high radiation swelling resistance [1]. They are elaborated via ball milling process, where germs of nano-oxides can be formed during this milling process or not depending on the milling conditions [2,3]. After milling, the powder is consolidated either by hot extrusion (>1000°C) or Hot Isostatic Pressuring treatment inducing nano-oxide formation. The nano-oxides remain very stable under high temperature and irradiation [4–7]. Under irradiation or after long time aging at temperature ranging between 400°C and 500°C, an unmixing α/ α′ of the matrix can be observed [4,8–15] depending on the initial Cr content. This unmixing leads to embrittlement of the material [15,16]. In Fe-Cr, the α' phase is known to be very sensitive to irradiation conditions, especially the damage rate [17,18] and implanted ions [19]. In ODS steels, the presence of numerous interfaces between the nano-oxides and the matrix, acting as sinks for point defects, may impact the formation of the α' phase and its dependency on the flux. The α' formation in a well-known ODS system thus needs to be investigated in details.

MA957, an oxide dispersion strengthened (ODS) steel developed by the International Nickel Company (INCO) with a nominal composition of Fe-13.7Cr-0.98Ti-0.3Mo-0.13Ni-0.03Al-0.25Y_2O_3 (wt.%) [5,20] was used in this study. The alloy is produced by a patented process known as mechanical alloying, which is a powder metallurgy milling process using high energy ball mills or attritors to homogeneously distribute alloying ingredients. Mechanically alloyed powders are subsequently consolidated by hot extrusion. The as-received material was cut into slices, mechanically thinned, and electro-polished [21].

Electro-polished samples were irradiated at 400°C for 20 hours with a raster beam of 12.5 MeV Fe^{5+} ions at JANNuS-Saclay (Figure 1a) [22]. The fluence was 5.2×10^{16} $Fe^{5+}.cm^{-2}$, corresponding to a dose of 5 dpa in the first 200 nm and 50 dpa at the damage peak (Figure 1b). Other samples were irradiated at 400°C with a raster beam of 5 MeV Fe^{3+} ions at JANNuS-Orsay [22] (Figure 1c), with a flux of 9×10^{10} $Fe^{3+}.cm^{-2}.s^{-1}$ and a fluence of 5.0×10^{15} $Fe^{3+}.cm^{-2}$. It corresponds to 5 dpa and 10^3 appm at peak damage

(Figure 1d). The damage depth profiles, calculated using Iradina [23] in quick calculation with a displacement energy of 40 eV, are shown in Figure 1 c & d.

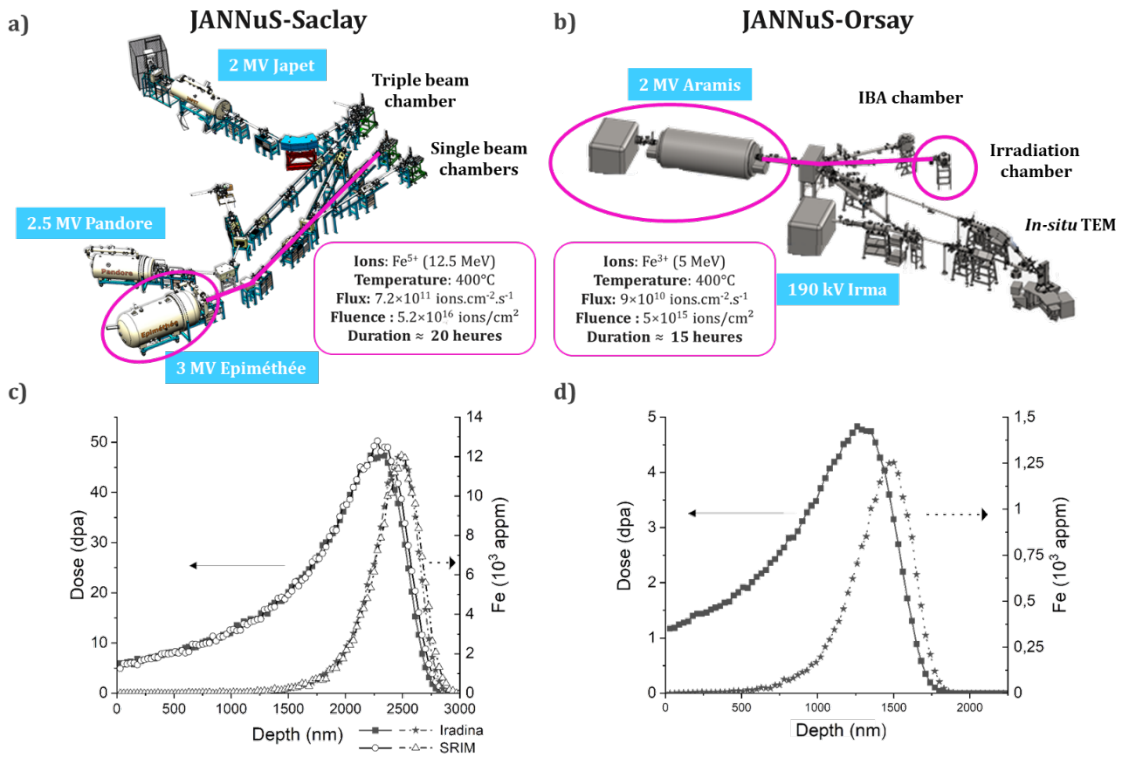

Figure 1: Schematic view of the JANNuS platforms with the beam lines used and the irradiation parameters, with (a) JANNuS-Saclay, and (b) JANNuS-Orsay, (c&d) Damage profiles calculated with Iradina(c&d) and SRIM (d) in quick calculation mode using a displacement energy for Fe of 40 eV for the irradiation at JANNuS-Saclay (c) and at JANNuS-Orsay (d).

Cross-section specimens for Transmission Electron Microscopy (TEM) and Atom Probe Tomography needles were lifted out and thinned using a Focused Ion Beam (FIB) equipped on a FEI Helio 650 NanoLab dual-beam Scanning Electron Microscope.

Energy Filtered TEM (EFTEM) and Energy Dispersive X-ray Spectroscopy (EDX) analysis were conducted on FIB thin foils. EFTEM Jump ratio images were obtained at Fe-$L_{2,3}$, Ti-$L_{2,3}$ and Cr-$L_{2,3}$ edges on a TECNAI FEI operating at 200kV and equipped with a Tridiem Gatan Imaging Filter (GIF). EDX analysis were performed on a TITAN3 G2 operating at 300kV equipped with a Bruker Super-X detector. EDX spectrum images were acquired and quantified using the Cliff-Lorimer correction.

APT analysis was performed using a CAMECA LEAP 4000XHR at 70 K in laser pulsing mode at a wavelength of 355 nm, 125 kHz pulse repetition rate and an energy between 32 and 35 pJ. 3D reconstruction, visualization and data post treatments were performed with the CAMECA IVAS Software. Profiles of chromium content were obtained along a cylinder of 2 nm radius and 30 nm^3 length using the algorithm 1D concentration profile with a fix bin of 1 nm. The α' particle volume is given by the IVAS isosurface algorithm with an isovalue of 25 at.%. The size and density of nano-oxides are extracted from the IVAS isosurface algorithm with an isovalue of 4 at.% of Y, YO, Ti and TiO. To characterize the Cr amplitude fluctuation, the variance s^2 of the observed frequency distribution, Oi, for a chromium concentration (i), is compared to the standard deviation σ^2 of a binomial distribution Bi (Equation 1). The scalar parameter V= $\sum_i |O_i - B_i|$ was also calculated with cubes of 300 atoms [24].

Equation 1 : Expression of the variance s^2 of an experimental distribution of chromium composition and the standard deviation of a binomial distribution centered on X_0. X_0: mean value of the frequency distribution of chromium composition, O_i: Composition of chromium in the cube i, N_b: Number of slices/cubes in the volume, n_b: Number of atoms per slice/cube.

$$s^2 = \frac{1}{N_b - 1}\sum_{i=1}^{N_b}(O_i - X_0) \qquad \sigma^2 = \frac{X_0(1 - X_0)}{n_b}$$

Table 1: MA957 composition in wt.% (nominal and determined by APT)

Element	Fe	Cr	Mo	Ti	Ni	Y	Mn	Al	O
Nominal	Bal.	13.7	0.3	0.98	0.13	0.20	0.09	0.03	0.05
APT	Bal.	13.74	0.30	0.74	0.33	0.19	0.06	0.02	0.11

The as-received material, MA957, is composed of elongated grains in the extrusion direction with a width of 250 nm and a length of 2 µm. Its composition was checked by APT (Table 1) and is close to its nominal composition except for the titanium content which is lower due to large micrometric titanium oxides in low density [5] that were not intercepted by APT.

MA957 exhibits a high density of nano-oxides, 2.6×10^{23} m^{-3}, with a mean radius of 1.3 ± 0.5 nm, which is coherent with the literature [5]. The nano-oxides are enriched in titanium and yttria as shown by APT

experiments (Figure 2 c1-c3). They can be imaged by EFTEM with an enrichment in titanium and a depletion of Cr and Fe (Figure 2 a-b).

Before irradiation, APT and EFTEM do not show any obvious local enrichment in Cr (Figure 2 a –c). The scalar parameter is $V_0 = 0.08$, and the variance s^2 of the Cr frequency distribution is close to the standard deviation σ^2 (Figure 2 d & e).

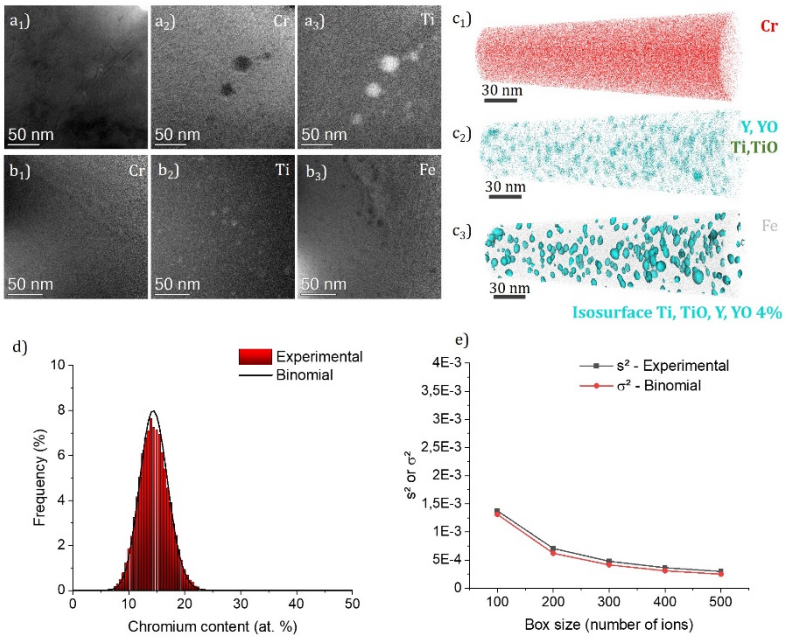

Figure 2: Analysis of MA957 steel before irradiation, by EFTEM (a_1, a_2, a_3, b_1, b_2, b_3) and APT (c_1, c_2, c_3, d, e). For EFTEM analysis, two different zones are imaged in pictures reported in (a_i) et (b_i): (a_1): Zero loss image of the first analyzed zone. (a_2 & b_1): Repartition of chromium for the two zones, (a_3 & b_2): Repartition of titanium, (b_3): Repartition of iron for the second analyzed zone. For APT analysis (c): Repartition of Cr ions in red, of Y, Ti, YO and TiO ions in blue, and of Fe ions in grey, respectively in (c_1), (c_2) and (c_3). In (c_3), the regions with a local concentration of Ti, TiO, Y and YO, higher than 4% (iso-surface) are highlighted in blue. (d) Histogram of chromium repartition inside the APT volume voxelized in 200 ions boxes, and the corresponding binomial distribution. (e) Variance of the chromium distribution s^2 (in d) and the corresponding binomial distribution (σ^2).

After irradiation at 400°C with 12.5 MeV Fe^{5+}, at a 300 nm depth, the chromium distribution deviates from the binomial distribution: the V parameter increases to 0.61 and s^2 diverges from σ^2 (Figure 3 b). By APT and EFTEM, local enrichments in chromium are detected (Figure 3). Chromium agglomerates away from nano-oxides: there is an obvious anticorrelation between the location of Cr precipitates and nano-oxides. The Cr precipitates are mostly composed of Fe and Cr (other element contents are lower than 0.1 %). The Cr content is 43.4 ± 0.1 at.% for an isosurface of 25% of Cr. The mean enrichment in

the center of particles ($1\times1\times1$ nm^3) is 54 ± 9 at.%. The Cr center enrichment depends on the particle size (Figure 4 c, red dots): the larger particles exhibit a higher chromium enrichment. The biggest particles, with a radius over 2.5 nm, have an enrichment of 75 at.% Cr as shown in Figure 3 c & d and Figure 4 c. The mean radius of Cr particles is estimated to be 2.2 ± 0.7 nm by APT, and 2.5 ± 1 nm by EFTEM (Figure 4 b). Their density is around $3 \pm 1\times10^{23}$ m^{-3}. The Cr matrix content, excluding Cr precipitates and nano-oxides, is around 13.4 ± 0.2%.

At the damage peak, the Cr is also less homogenously distributed than before irradiation, with V = 0.24. Local enrichments of Cr are seen by APT, STEM-EDS and EFTEM (Figure 4 a & d, areas 4 and 4'). But the radius and the density of Cr precipitates estimated by APT, respectively of 1.5 ± 0.32 nm and $\sim1\times10^{22}$ m^{-3}, are lower than at 300 nm. The average and the core Cr composition of Cr particles is ~37 ± 0.5 at.% and 42 ± 6 at.%, respectively. The Cr enrichment at the center of particles has the same dependence on particle radius at 2250 nm and at 300 nm (Figure 4 c). EFTEM experiments on several regions and thin foils showed that Cr enrichments are always obvious from the surface up to around 1800 nm in depth, and more difficult to observe beyond. In particular, Cr particles are more obvious at a depth of 1800 nm than at 2500 nm (see Figure 4 d in areas 3, 3' and 5, 5'), whereas, according to calculations, the damage is the same. The main difference is the implanted atom concentration, which amounts to 1×10^3 appm and 12×10^3 appm at 1800 and 2500 nm, respectively.

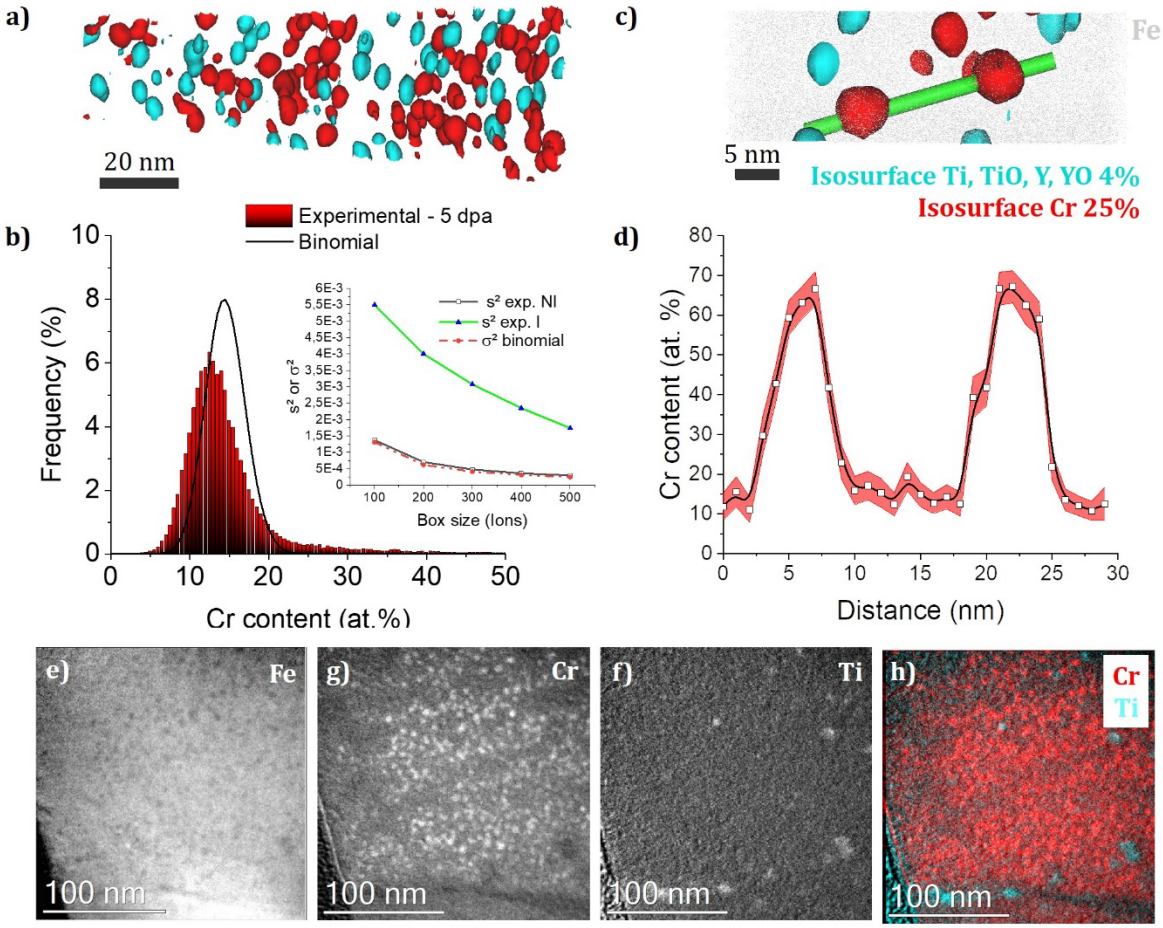

Figure 3: Analysis of MA957 steel after irradiation at 400°C with 12.5 MeV Fe^{5+} at 5.2×10^{16} $Fe^{5+}.cm^{-2}$ by APT (a,c) and by ETEM (e-h). **APT:** (a & c): Isosurface with 25% of chromium in red and with 4 % of Ti, TiO, Y, YO in blue. The Fe ions are in grey. (b) Histogram of chromium repartition inside the APT volume voxelized in 200 ions boxes and the corresponding binomial distribution. On the right, variance of the chromium distribution by APT before (s^2 NI, in black) and after irradiation (s^2 I, in green) and the corresponding binomial distribution (σ^2, in red). (d): Profile of chromium composition along the green cylinder in (c) going across two enriched regions in chromium. The red shaded area represents the statistical error associated with the measurement of the composition. **EFTEM:** (e-h): Repartition of Fe, Cr, Ti, respectively in (e), (f), (g). (h): Overlap of repartition of chromium in red and titanium in blue.

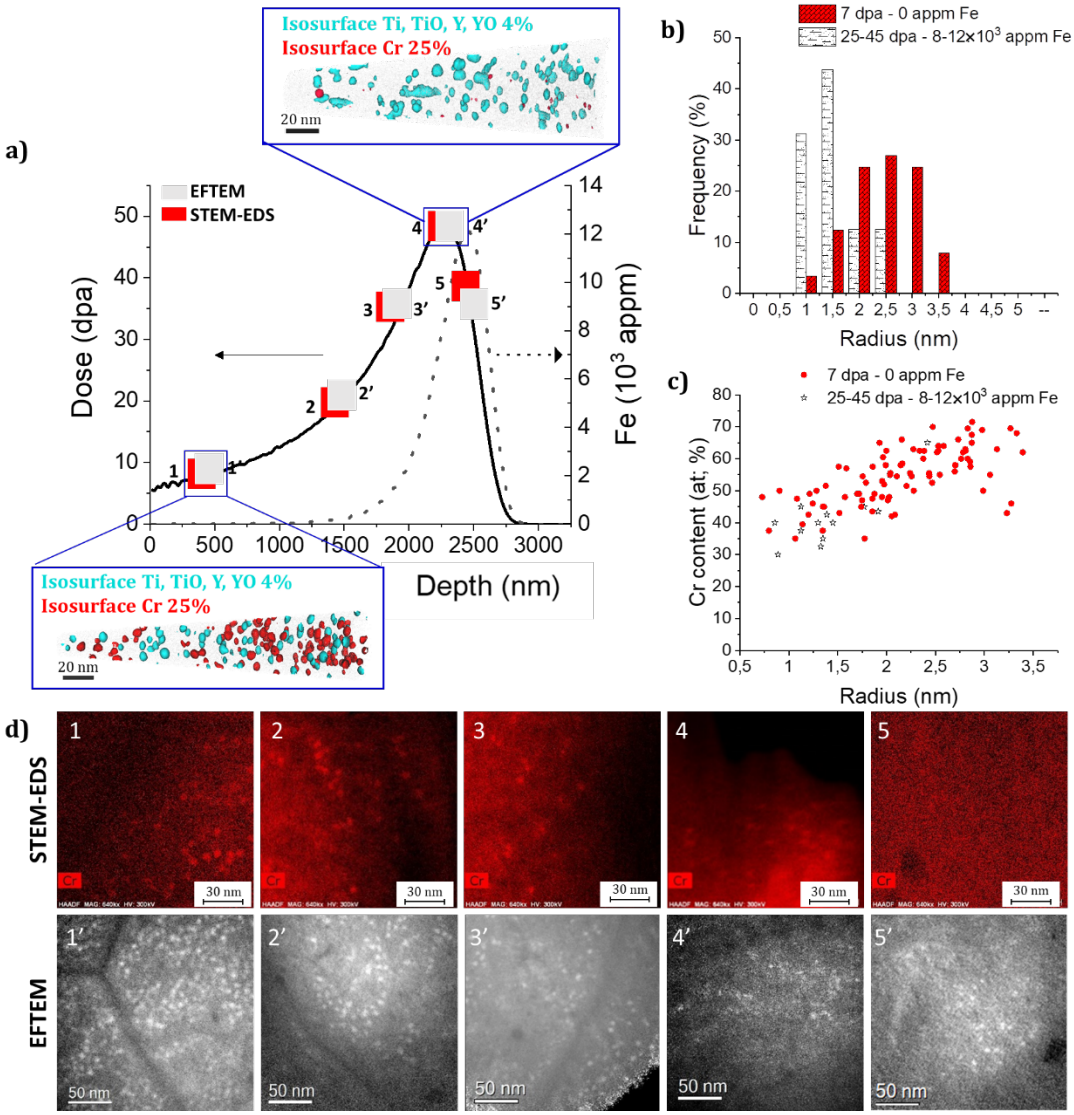

Figure 4: Analysis of MA957 steel after irradiation at 400°C with 12.5 MeV Fe at 5.2×10^{16} $Fe^{5+}.cm^{-2}$ along the damage profile by EFTEM, STEM-EDS and APT. (a) Damage and implanted ion profiles along the irradiation depth with APT analysis for two depth: 500 nm and 2000 nm. Fe ions are in grey, 4 % isosurface of Ti, TiO, Y, YO in blue and 25 % isosurface of Cr in red. Selected areas analyzed by EFTEM and STEM-EDS are located on the damage depth profile and numbered from 1,1' to 5, 5'. (b) Frequency distribution of α' precipitate radius obtained by APT for 2 irradiation depths: 500 nm in red and 2200 nm in white. (c) Cr content in the core (1 nm^3) of α' precipitates obtained by APT as a function of their radius for two irradiation depths: 500 nm in red dots and 2200 nm in white stars. (d) Repartition of Cr obtained by EFTEM (in grey) and STEM-EDS in red for the 5 depths indicated in (a).

The phase diagram of the MA957 is unknown due to chemical complexity. For a simple approach, the ODS matrix can be considered as an $Fe_{85.4}Cr_{14.6}$ alloy for which the phase diagram is better known [25]. The Cr solubility limit at 400°C was given at 8.3 at.% [11] and 10.5 at.% [26]. Above, a Cr-rich α' phase

is expected [11,25,26]. One can argue that the chemical complexity of ODS steels could change the solubility limit of α' formation as reported for ODS steels with or without aluminum [14,27]. Even though α' formation was not formally reported after thermal annealing at 400°C in MA957, it was observed for two 14 wt.% Cr ODS steels, after annealing at 400°C (5000 h and 10000 h) [13] and 475°C (9000 h) [14]. α' formation should also be thermodynamically favorable for MA957 after annealing at 400°C, as suggested by Bailey et al. [9]. Here, the Cr-rich precipitates observed after irradiation at 400°C do not contain other element than Fe and Cr (no C, nor O), and consequently, they must be α' precipitates. As no α' precipitates are observed away from the irradiation zone, irradiation drastically accelerates α' formation.

α′ was observed in MA957 after ion [10] and neutron irradiation [9,11,12,28]. The precipitate size and density, r = 2.1± 0.1 nm and d = 9×10^{23} m^{-3}, reported by Bailey et al. [9] after neutron irradiation at 109 dpa and 412°C is rather close to the ones we found at 7 dpa with 12.5 MeV Fe^{5+}. Aydogan et al. also reported similar size and density (3.37 ± 0.85 nm and 4.97 ± 0.99×10^{23} m^{-3}) after neutron irradiation at 7 dpa and 360-370°C for an 15.2Cr-0.92W-0.47Ti-0.13Y-Fe (at.%) ODS steel [29]. Moreover, the chromium content of α' determined by APT for an isosurface of 25 at.% (42 ± 6 at.%) is very similar to the one found after neutron irradiation at 412°C (41 ± 1 at. %) also for an isosurface of 25 at.% in APT [9]. Therefore, it seems that the flux and fluence do not influence much the α' precipitate characteristics. It could be due to a stationary regime resulting from a balance between an irradiation/ballistic dissolution and a precipitation accelerated by irradiation.

Figure 4c shows that the core chromium content depends on the particle size. Hatzouglou et al. [30] showed that above a radius of 1 nm, the core chromium content of α' is not no influenced by any APT aberrations and should be reliable. Here, the analyzed precipitates are larger than 1 nm in radius, so the chromium content indeed increases with the size of α′ precipitates and therefore duration of precipitation. This characteristic had already been seen by Chen et al. [31] in an $Fe_{90}Cr_{10}$ irradiated with neutrons at 450°C and 1 dpa. Interestingly, α′ precipitates formed in MA957 irradiated with 12.5 MeV Fe^{5+} at depths of 500 nm and 2.2 μm have the same Cr content dependency with size (Figure 4c). It indicates that the same phase is formed at both depths. As the particles are denser and larger at 500 nm

(5 dpa, 7×10^{-5} dpa/s), the precipitation seems to be less advanced at 2.2 µm (45 dpa, 6×10^{-4} dpa/s) even if the damage is 9 times more important. Three factors can explain this phenomenon: the damage rate, the dose or the implanted ions.

The damage rate would influence precipitation through ballistic mixing mostly. Ballistic mixing causes a redistribution of Cr atoms, potentially inducing a reduction of precipitate size and chromium content. For very high damage rates, the redistribution of Cr atoms induced by ballistic mixing may even prevent α' formation [17,18,32], as shown in $Fe_{85}Cr_{15}$ above 1×10^{-4} dpa/s at 400°C [32]. Here, the α' core chromium content (55 ± 9 at.%) and α' chromium content dependency with the particle size are identical to the ones reported by Chen et al. in an Fe_{90}-Cr_{10} (55 at.%) irradiated with neutrons at 450°C and 1 dpa [31]. These similarities suggest that the α' particles formed in both materials and irradiation conditions are similar. The α' chromium content increases with the size of precipitates and therefore duration of precipitation. It seems to saturate around 70 at.% for precipitates with a radius exceeding 2.5 nm. This value is close to the ones found for large α' particles (> 5 nm in radius) formed in 15 at.% Cr ODS steels after thermal annealing at 450°C for 5000h (70-80 at.%) [13] and 475°C for 9000h (75 at.%) [14]. The chromium concentration in large α' particles is thus the same after neutron, ion irradiation and thermal annealing, and therefore, ballistic mixing doesn't seem to occur with significant effects.

The second factor that can induce a lower precipitation of the α′ at 2.2 µm is the increase of dose. Indeed, Soisson et al. [33] showed that the sink strength increases with dose. This increase reduces the point defects saturation and exacerbates the effect of ballistic dissolution, reducing the α' precipitate density and size. But in the present case, there is no sign of ballistic dissolution at a depth of 1.7–1.9 µm (dose 35 dpa, damage rate 4×10^{-4} dpa/s), and an influence of the dose is thus also unlikely. It is equally unlikely that a factor of 1.4, by which the dose and damage rate vary between 1.9 and 2.2 µm, is responsible for the observed large differences in precipitation.

The adopted hypothesis is therefore the influence of injected ions, which constitute the main difference between depths of 1.9 µm and 2.5 µm for which the precipitation strongly differs (Figure 4 areas 3 and 5). To confirm this hypothesis, a sample of MA957 was irradiated at 400°C with 5 MeV Fe^{3+}. The dose, ~ 5 dpa, and flux, 8.3×10^{-5} dpa/s, at the damage peak, were selected to closely match those achieved

within a 250 nm surface layer of samples irradiated with 12.5 MeV Fe^{5+} (Figure 5 a & b). Figure 5 shows the difference between the two irradiations and highlights the influence of the implanted ions, which was already evidenced in an $Fe_{85}Cr_{15}$ after ion irradiation [19]. Cr precipitates can easily be characterized by EFTEM at 5 dpa without implanted ions for the 12.5 MeV Fe^{5+} irradiation (Figure 5 a, a1-a3), whereas no Cr precipitates are seen at 5 dpa with 10^3 appm of Fe for the 5 MeV Fe^{3+} irradiation (Figure 5 b, b1-b3).

The injected ions are assumed to trigger the formation of a high density of small sinks such as small clusters [33,34], increasing the sink strength at the damage peak, and leading to a smaller point defects sursaturation [33]. This either delays α' precipitation, or induces a stronger ballistic dissolution.

Interestingly, the ballistic mixing seems to be less pronounced in ODS-steels than in Fe-Cr. Indeed no ballistic dissolution is seen for a damage rate of 2×10^{-4} dpa/s whereas Thomas et al. [32] showed a complete α' dissolution above 10^{-4} dpa/s. The main difference between Fe-Cr and ODS lies in the presence of nano-oxides precipitates, but this cannot account for the reduced ballistic mixing in ODS steels. Since the nano-oxides act as sinks for point defects, they should reduce point defect concentration and thus Cr diffusion [35]. A higher ballistic mixing would therefore be expected for ODS steels compared to Fe-Cr alloys. Two hypotheses could explain this phenomenon: a reduced point defect concentration in Fe-Cr due to a high density of loops, or a higher Cr diffusion in ODS steels. The first one is unlikely, as it would require a loop density in Fe-Cr largely exceeding the nano-oxides density (2.6×10^{23} m^{-3}) in MA957. Porollo et al. reported a loop density of 2×10^{22} m^{-3} and 3×10^{22} m^{-3} after neutron irradiation at 400°C to 5-7 dpa for a Fe-12wt%Cr and a Fe-18wt%Cr, respectively [36]. Alternatively, an accelerated chromium diffusion in MA957 could be due to the presence of oxygen and its affinity with Cr and vacancies [37]. If such is the case, our study suggests that it is crucial to control and limit oxygen contamination in ODS steels to delay the appearance of the α' phase and ensure the integrity of ODS components in future reactors.

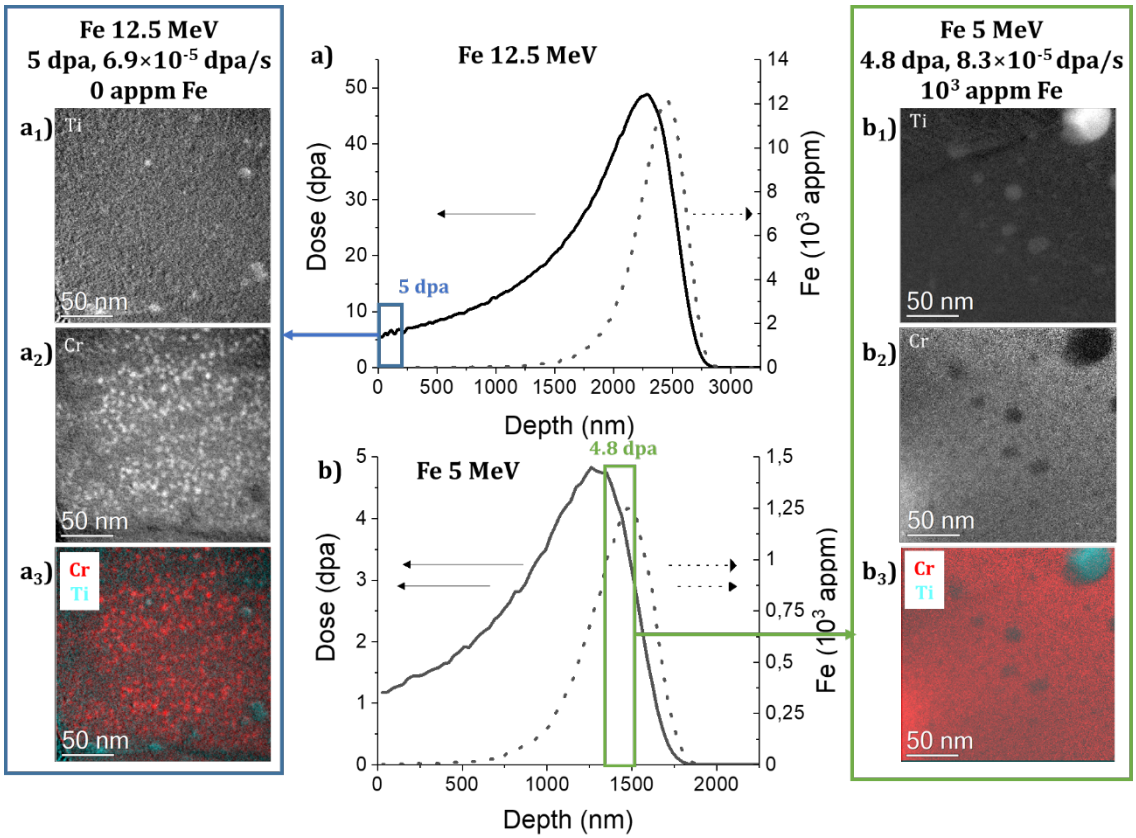

Figure 5: Impact of Fe implantation on α' precipitation in an MA957 ODS. (a) Damage and implanted ion profiles along the irradiation depth for 12.5 MeV Fe^{5+} ions at 5.2×10^{16} $Fe^{5+}.cm^{-2}$. Titanium (a_1), Chromium (a_2) and superposition of chromium (in red) and titanium (in blue) (a_3) repartitions obtained by EFTEM in a MA957 in the first 200 nm corresponding to a dose of 5 dpa after irradiation with 12.5 MeV Fe^{5+}. (b) Damage and implanted ion profiles along the irradiation depth for 5MeV Fe^{3+} ions at 4.9×10^{15} $Fe^{3+}.cm^{-2}$. Titanium (b_1), Chromium (b_2) and superposition of chromium (in red) and titanium (in blue) (b_3) repartitions obtained by EFTEM in a MA957 after irradiation with 5 MeV Fe^{3+} at 4.9×10^{15} $Fe^{3+}.cm^{-2}$ at a depth of 1500 nm, corresponding to a dose of 4.8 dpa and 10^3 appm of implanted Fe.

In conclusion, MA957 exhibits a strong α' precipitation after ion irradiation at 400°C. The characteristics of the α' phase are rather close to the ones obtained after neutron irradiation and after thermal annealing of Fe-Cr and 15 at.% Cr ODS steels, which suggests that ion irradiation only accelerates precipitation. For the first time to our knowledge, the influence of implanted ions on the α' formation is revealed in an ODS steel. Implanted ions drastically inhibit α' formation: for the same dose rate and fluence, the density and size of the α' phase are reduced. This suggests that the implanted ions either reduce the fraction of α' phase formed after irradiation or delay considerably its formation. Lastly, no ballistic dissolution of α' is observed, in contrast with Fe-Cr systems irradiated in similar conditions.

Acknowledgement:

The research was supported by the Cross-cutting basic research Program of Division Energy of CEA (RTA Program), the RMATE project (CEA), and by the French government, managed by the French National Research Agency, under the "Investissements d'avenir" program (No. ANR-11-EQPX-0020). This work has been carried out within the framework of the French Federation for Fusion and EUROfusion Consortium and has received funding from the Euratom research and training program (WPEDU) 2019-2020 under grant agreement No 633053. The views and opinions expressed herein do not necessarily reflect those of the European Commission. The irradiation experiments were supported by the French EMIR&A accelerators network. The authors are grateful to the JANNuS-Saclay and the JANNuS-Orsay experimental hall teams for performing ions irradiation. The authors acknowledge the inspiring discussion on mechanisms with Maylise Nastar and Frédéric Soisson in SRMP/CEA-Saclay.

[1] J.-L. Séran, M. Le Flem, 8 - Irradiation-resistant austenitic steels as core materials for Generation IV nuclear reactors, in: P. Yvon (Ed.), Structural Materials for Generation IV Nuclear Reactors, Woodhead Publishing, 2017: pp. 285–328. https://doi.org/10.1016/B978-0-08-100906-2.00008-2.

[2] M. Loyer-Prost, J.-S. Merot, J. Ribis, Y. Le Bouar, L. Chaffron, F. Legendre, High resolution Transmission Electron Microscopy characterization of a milled oxide dispersion strengthened steel powder, Journal of Nuclear Materials 479 (2016). https://doi.org/10.1016/j.jnucmat.2016.06.050.

[3] M. Laurent-Brocq, F. Legendre, M.-H. Mathon, A. Mascaro, S. Poissonnet, B. Radiguet, P. Pareige, M. Loyer, O. Leseigneur, Influence of ball-milling and annealing conditions on nanocluster characteristics in oxide dispersion strengthened steels, Acta Materialia 60 (2012) 7150–7159. https://doi.org/10.1016/j.actamat.2012.09.024.

[4] J. Ribis, S. Lozano-Perez, Nano-cluster stability following neutron irradiation in MA957 oxide dispersion strengthened material, Journal of Nuclear Materials 444 (2014) 314–322. https://doi.org/10.1016/j.jnucmat.2013.10.010.

[5] H. Sakasegawa, F. Legendre, L. Boulanger, M. Brocq, L. Chaffron, T. Cozzika, J. Malaplate, J. Henry, Y. [de Carlan, Stability of non-stoichiometric clusters in the MA957 ODS ferrtic alloy, Journal of Nuclear Materials 417 (2011) 229–232. https://doi.org/10.1016/j.jnucmat.2010.12.056.

[6] E. Aydogan, N. Almirall, G.R. Odette, S.A. Maloy, O. Anderoglu, L. Shao, J.G. Gigax, L. Price, D. Chen, T. Chen, F.A. Garner, Y. Wu, P. Wells, J.J. Lewandowski, D.T. Hoelzer, Stability of nanosized oxides in ferrite under extremely high dose self ion irradiations, Journal of Nuclear Materials 486 (2017) 86–95. https://doi.org/10.1016/j.jnucmat.2017.01.015.

[7] J. Ribis, F. Delabrouille, J. Malaplate, Stability of nano-oxides upon heavy ion irradiation of an ODS material, Journal of Nuclear Materials (2011). https://doi.org/10.1016/j.jnucmat.2010.12.068.

[8] E. Aydogan, E. Martinez, K. March, O. El-Atwani, D.L. Krumwiede, P. Hosemann, T. Saleh, S.A. Maloy, α′ formation kinetics and radiation induced segregation in neutron irradiated 14YWT

nanostructured ferritic alloys, Scientific Reports 9 (2019) 8345. https://doi.org/10.1038/s41598-019-44508-5.
[9] N.A. Bailey, E. Stergar, M. Toloczko, P. Hosemann, Atom probe tomography analysis of high dose MA957 at selected irradiation temperatures, Journal of Nuclear Materials 459 (2015) 225–234. https://doi.org/10.1016/j.jnucmat.2015.01.006.
[10] J. Wang, M.B. Toloczko, V.N. Voyevodin, V.V. Bryk, O.V. Borodin, V.V. Mel'nychenko, A.S. Kalchenko, F.A. Garner, L. Shao, Atom probe tomography characterization of high-dose ion irradiated MA957, Journal of Nuclear Materials 545 (2021) 152528. https://doi.org/10.1016/j.jnucmat.2020.152528.
[11] M.H. Mathon, Y. de Carlan, G. Geoffroy, X. Averty, A. Alamo, C.H. de Novion, A SANS investigation of the irradiation-enhanced α–α′ phases separation in 7–12 Cr martensitic steels, Journal of Nuclear Materials 312 (2003) 236–248. https://doi.org/10.1016/S0022-3115(02)01630-6.
[12] D.S. Gelles, Microstructural examination of commercial ferritic alloys at 200 dpa, Journal of Nuclear Materials 233–237 (1996) 293–298. https://doi.org/10.1016/S0022-3115(96)00222-X.
[13] M.M. Issaoui, Amal, Comportement sous irradiation des aciers ODS (Oxide Dispersion Strengthened) pour le gainage combustible des réacteurs de 4ème génération, Université Lille, 2021.
[14] P. Dou, Effects of the contents of Al, Ti, W and Y2O3 on long-term thermal ageing behavior of 15Cr ODS ferritic steels, Journal of Nuclear Materials (2020) 152129. https://doi.org/10.1016/j.jnucmat.2020.152129.
[15] A.-L. Rouffié, Compréhension et modélisation de la rupture fragile des aciers renforcés par nano-précipitation : effets de texture, de vieillissement et de composition, 2014.
[16] P.J. Grobner, The 885° f (475° c) embrittlement of ferritic stainless steels, Metallurgical Transactions 4 (1973) 251–260.
[17] J.-H. Ke, E.R. Reese, E.A. Marquis, G.R. Odette, D. Morgan, Flux effects in precipitation under irradiation – Simulation of Fe-Cr alloys, Acta Materialia 164 (2019) 586–601. https://doi.org/10.1016/j.actamat.2018.10.063.
[18] E.R. Reese, N. Almirall, T. Yamamoto, S. Tumey, G. Robert Odette, E.A. Marquis, Dose rate dependence of Cr precipitation in an ion-irradiated Fe18Cr alloy, Scripta Materialia 146 (2018) 213–217. https://doi.org/10.1016/j.scriptamat.2017.11.040.
[19] O. Tissot, C. Pareige, E. Meslin, B. Décamps, J. Henry, Influence of injected interstitials on α′ precipitation in Fe–Cr alloys under self-ion irradiation, Materials Research Letters 5 (2017) 117–123. https://doi.org/10.1080/21663831.2016.1230896.
[20] H. Sakasegawa, L. Chaffron, F. Legendre, L. Boulanger, T. Cozzika, M. Brocq, Y. de Carlan, Correlation between chemical composition and size of very small oxide particles in the MA957 ODS ferritic alloy, Journal of Nuclear Materials 384 (2009) 115–118. https://doi.org/10.1016/j.jnucmat.2008.11.001.
[21] M. Loyer-Prost, C. Hatzoglou, B. Radiguet, G. Vaux, D. Nunes, D. Sornin, N. Lochet, P.-F. Giroux, F. Frossard, Y. Le Bouar, S. Poissonnet, P. Bonnallie, P. Pareige, L. Chaffron, F. Legendre, Influence of milling duration and aluminum pollution on the microstructure of oxide dispersion strengthened, International Congress on Advances in Nuclear Power Plants, ICAPP 2014 3 (2014) 2116–2125.
[22] A. Gentils, C. Cabet, Investigating radiation damage in nuclear energy materials using JANNuS multiple ion beams, Nuclear Instruments and Methods in Physics Research Section B: Beam Interactions with Materials and Atoms 447 (2019) 107–112. https://doi.org/10.1016/j.nimb.2019.03.039.
[23] J.-P. Crocombette, C. Wambeke, Quick calculation of damage for ion irradiation: implementation in Iradina and comparisons to SRIM, EPJ N - Nuclear Sciences & Technologies 5 (2019) 7. https://doi.org/10.1051/epjn/2019003.
[24] F. Danoix, P. Auger, D. Blavette, Hardening of Aged Duplex Stainless Steels by Spinodal Decomposition, Microsc Microanal 10 (2004) 349–354. https://doi.org/10.1017/S1431927604040516.

[25] M. Levesque, E. Martınez, C.-C. Fu, M. Nastar, F. Soisson, Simple concentration-dependent pair interaction model for large-scale simulations of Fe-Cr alloys, Physical Review B 84 (2011) 184205. https://doi.org/10.1103/PhysRevB.84.184205.
[26] G. Bonny, D. Terentyev, L. Malerba, New Contribution to the Thermodynamics of Fe-Cr Alloys as Base for Ferritic Steels, 31 (2010) 439–444. https://doi.org/10.1007/s11669-010-9782-9.
[27] W. Li, S. Lu, Q.-M. Hu, H. Mao, B. Johansson, L. Vitos, The effect of Al on the 475°C embrittlement of Fe–Cr alloys, Computational Materials Science 74 (2013) 101–106. https://doi.org/10.1016/j.commatsci.2013.03.021.
[28] J. Ribis, S. Lozano-Perez, Orientation relationships and interface structure of α′-Cr nanoclusters embedded in α-Fe matrix after α–α′ demixing in neutron irradiated Oxide Dispersion Strengthened material, Materials Letters 74 (2012) 143–146. https://doi.org/10.1016/j.matlet.2012.01.115.
[29] E. Aydogan, J.S. Weaver, U. Carvajal-Nunez, M.M. Schneider, J.G. Gigax, D.L. Krumwiede, P. Hosemann, T.A. Saleh, N.A. Mara, D.T. Hoelzer, B. Hilton, S.A. Maloy, Response of 14YWT alloys under neutron irradiation: A complementary study on microstructure and mechanical properties, Acta Materialia 167 (2019) 181–196. https://doi.org/10.1016/j.actamat.2019.01.041.
[30] C. Hatzoglou, B. Radiguet, G. Da Costa, P. Pareige, M. Roussel, M. Hernandez-Mayoral, C. Pareige, Quantification of APT physical limitations on chemical composition of precipitates in Fe–Cr alloys, Journal of Nuclear Materials 522 (2019) 64–73. https://doi.org/10.1016/j.jnucmat.2019.05.022.
[31] W.-Y. Chen, Y. Miao, Y. Wu, C.A. Tomchik, K. Mo, J. Gan, M.A. Okuniewski, S.A. Maloy, J.F. Stubbins, Atom probe study of irradiation-enhanced α′ precipitation in neutron-irradiated Fe–Cr model alloys, Journal of Nuclear Materials 462 (2015) 242–249. https://doi.org/10.1016/j.jnucmat.2015.04.005.
[32] K.N. Thomas, Effect of cascade size and damage rate on α' precipitate stability in Fe-15Cr, Journal of Nuclear Materials 585 (2023) 154615. https://doi.org/10.1016/j.jnucmat.2023.154615.
[33] F. Soisson, E. Meslin, O. Tissot, Atomistic modeling of α' precipitation in Fe-Cr alloys under charged particles and neutron irradiations: Effects of ballistic mixing and sink densities, Journal of Nuclear Materials 508 (2018) 583–594. https://doi.org/10.1016/j.jnucmat.2018.06.015.
[34] F. Soisson, T. Jourdan, Radiation-accelerated precipitation in Fe–Cr alloys, Acta Materialia 103 (2016) 870–881. https://doi.org/10.1016/j.actamat.2015.11.001.
[35] O. Senninger, F. Soisson, E. Martínez, M. Nastar, C.-C. Fu, Y. Bréchet, Modeling radiation induced segregation in iron–chromium alloys, Acta Materialia (2016).
[36] S.I. Porollo, A.M. Dvoriashin, A.N. Vorobyev, Y.V. Konobeev, The microstructure and tensile properties of Fe±Cr alloys after neutron irradiation at 400°C to 5.5±7.1 dpa, Journal of Nuclear Materials (1998).
[37] A.J. Samin, Ab initio based examination of the kinetics and thermodynamics of oxygen in Fe-Cr alloys, Physical Review B 99 (2019) 174202. https://doi.org/10.1103/PhysRevB.99.174202.